A NUMERICAL STUDY OF THE SELF-SIMILAR SOLUTIONS OF THE SCHRÖDINGER MAP

F. DE LA HOZ[*], C. GARCíA-CERVERA[†], AND L. VEGA[‡]

Abstract. *We present a numerical study of the self-similar solutions of the Localized Induction Approximation of a vortex filament. These self-similar solutions, which constitute a one-parameter family, develop a singularity at finite time. We study a number of boundary conditions that allow us reproduce the mechanism of singularity formation. Some related questions are also considered.*

Key words. Collocation Methods, Numerical Analysis of PDE's, Formation of Singularities, Localized Induction Approximation, Schrödinger-type equations

AMS subject classifications. 35Q55, 65D10, 65N35, 65T50, 76B47

1. Introduction. Given a curve $\mathbf{X}_0 : \mathbb{R} \longrightarrow \mathbb{R}^3$, consider the geometric flow

$$\mathbf{X}_t = c\mathbf{b}, \tag{1.1}$$

where c is the curvature and $\mathbf{b}$ the binormal component of the Frenet-Serret formulae

$$\begin{pmatrix} \mathbf{T} \\ \mathbf{n} \\ \mathbf{b} \end{pmatrix}_s = \begin{pmatrix} 0 & c & 0 \\ -c & 0 & \tau \\ 0 & -\tau & 0 \end{pmatrix} \cdot \begin{pmatrix} \mathbf{T} \\ \mathbf{n} \\ \mathbf{b} \end{pmatrix}. \tag{1.2}$$

The flow can be expressed as

$$\mathbf{X}_t = \mathbf{X}_s \wedge_+ \mathbf{X}_{ss}, \tag{1.3}$$

where $\wedge_+$ is the usual cross-product, and s denotes arclength. This flow appeared for the first time in 1906 [10] and was rederived in 1965 by Arms and Hama [1] as an approximation of the dynamics of a vortex filament under the Euler equations. This model is usually known as the Localized Induction Approximation (LIA). We refer the reader to [5] and [26] for an analysis and discussion about the limitations of this model. Starting with the work of Schwartz in [27], the LIA has been also used as an approximation of the quantum vortex motion in superfluid Helium. Of particular relevance for our purposes is the recent work of T. Lipniacki [24], [25]. A rather complete list of references about the use of LIA in this setting can be found in these two papers.

Some of the explicit solutions of (1.3) are the line, circle and helix. It is easy to see that the tangent vector $\mathbf{T} = \mathbf{X}_s$ remains with constant length, so that we can assume that it takes values on the unit sphere. Differentiating (1.3), we get the following equation for $\mathbf{T}$:

$$\mathbf{T}_t = \mathbf{T} \wedge_+ \mathbf{T}_{ss}. \tag{1.4}$$

---

[*]Departamento de Matemática Aplicada, Universidad del País Vasco-Euskal Herriko Unibertsitatea. Partially supported by grant MTM2007-62186

[†]Mathematics Department, University of California, Santa Barbara, CA 93106, USA. Partially supported by NSF grant DMS-0505738.,

[‡]Departamento de Matemáticas, Universidad del País Vasco-Euskal Herriko Unibertsitatea. Partially supported by grant MTM2007-62186

This equation, known as the Schrödinger map equation on the sphere, is a particular case of the Landau-Lifshitz equation for ferromagnetism [23] and can be rewritten in a more geometric way as

$$\mathbf{T}_t = \mathbf{J}\mathbf{D}_s\mathbf{T_s}, \tag{1.5}$$

where $\mathbf{D}$ is the covariant derivative and $\mathbf{J}$ is the complex structure of the sphere. Written in this way, (1.4) admits an immediate generalization and we can change both its definition domain (considering for instance more variables) and its image (considering other more complex varieties). We will insist on the second possibility, choosing also the hyperbolic plane $\mathbb{H}^2$ as the target space; in that case, the equation for $\mathbf{T}$ is

$$\mathbf{T}_t = \mathbf{T} \wedge_- \mathbf{T}_{ss} \tag{1.6}$$

and, equivalently, for $\mathbf{X}$,

$$\mathbf{X}_t = \mathbf{X}_s \wedge_- \mathbf{X}_{ss}, \tag{1.7}$$

with $\wedge_-$ defined as

$$\mathbf{a} \wedge_- \mathbf{b} = (a_2b_3 - a_3b_2, a_3b_1 - a_1b_3, -(a_1b_2 - a_2b_1)).$$

In this article, we study numerically the self-similar solutions of

$$\mathbf{X}_t = \mathbf{X}_s \wedge_\pm \mathbf{X}_{ss}. \tag{1.8}$$

where $\wedge_\pm$ has been defined as

$$\mathbf{a} \wedge_\pm \mathbf{b} = (a_2b_3 - a_3b_2, a_3b_1 - a_1b_3, \pm(a_1b_2 - a_2b_1)).$$

Equivalently, a generalized version of the scalar product, denoted by $\circ_\pm$, is given as

$$\mathbf{a} \circ_\pm \mathbf{b} = a_1b_1 + a_2b_2 \pm a_3b_3.$$

By using $\pm$, we can consider simultaneously the Euclidean case, corresponding to $+$ and the Hyperbolic case, corresponding to $-$. Equivalently, whenever we use $\mp$, the $-$ sign will refer to the Euclidean case and the $+$ sign to the Hyperbolic one. Using the $\wedge_\pm$ notation, the equation for $\mathbf{X}_s = \mathbf{T}$ is now

$$\mathbf{T}_t = \mathbf{T} \wedge_\pm \mathbf{T}_{ss}. \tag{1.9}$$

If $\mathbf{T} \in \mathbb{H}^2$, it is still possible to give a generalized version of the Frenet-Serret trihedron (1.2) for each point of the curve $\mathbf{X}$, formed by $\mathbf{T}$ and two other vectors $\mathbf{e}_1$ and $\mathbf{e}_2$. Indeed, a few calculations show that, for both cases, all the possible generalizations of (1.2) have the form

$$\begin{pmatrix} \mathbf{T} \\ \mathbf{e}_1 \\ \mathbf{e}_2 \end{pmatrix}_s = \begin{pmatrix} 0 & \alpha & \beta \\ \mp\alpha & 0 & \delta \\ \mp\beta & -\delta & 0 \end{pmatrix} \cdot \begin{pmatrix} \mathbf{T} \\ \mathbf{e}_1 \\ \mathbf{e}_2 \end{pmatrix}, \tag{1.10}$$

where $\mathbf{T} \circ_\pm \mathbf{T} = \pm 1$, $\mathbf{e}_1 \circ_\pm \mathbf{e}_1 = \mathbf{e}_2 \circ_\pm \mathbf{e}_2 = 1$, $\mathbf{T} \circ_\pm \mathbf{e}_1 = \mathbf{T} \circ_\pm \mathbf{e}_2 = \mathbf{e}_1 \circ_\pm \mathbf{e}_2 = 0$; with regard to $\wedge_\pm$, we have $\mathbf{T} \wedge_\pm \mathbf{e}_1 = \mathbf{e}_2$, $\mathbf{e}_1 \wedge_\pm \mathbf{e}_2 = -\mathbf{T}$, $\mathbf{e}_1 \wedge_\pm \mathbf{e}_2 = \pm\mathbf{T}$. Without loss

of generality, we can choose one of the coefficients α, β or δ to equal zero. If we make $\beta = 0$ and denote $\alpha \equiv c$ and $\delta \equiv \tau$, (1.10) becomes

$$\begin{pmatrix} \mathbf{T} \\ \mathbf{e}_1 \\ \mathbf{e}_2 \end{pmatrix}_s = \begin{pmatrix} 0 & c & 0 \\ \mp c & 0 & \tau \\ 0 & -\tau & 0 \end{pmatrix} \cdot \begin{pmatrix} \mathbf{T} \\ \mathbf{e}_1 \\ \mathbf{e}_2 \end{pmatrix}. \tag{1.11}$$

In the Euclidean case, $\mathbf{e}_1$ and $\mathbf{e}_2$ refer to $\mathbf{n}$ and $\mathbf{b}$ respectively. In the hyperbolic case, we can refer to c and τ as the generalized curvature and torsion. In both cases, it is possible to recover $\mathbf{X}$, except for some rigid motion, if c and τ are known.

The self-similar solutions of (1.8) have been studied in [19] in the Euclidean case and in [11] in the hyperbolic one -see also [24], [25] for some related work. They are such that if $\mathbf{X}(s,t)$ solves (1.8), so does $\lambda^{-1}\mathbf{X}(\lambda s, \lambda^2 t)$. Therefore, taking $\lambda = t^{-1/2}$ and defining $\mathbf{G}(s) = \mathbf{X}(s,1)$, the self-similar solutions will be of the form

$$\mathbf{X}(s,t) = t^{1/2}\mathbf{X}(t^{-1/2}s,1) = \sqrt{t}\mathbf{G}(s/\sqrt{t}). \tag{1.12}$$

Bearing this in mind, after some straightforward but tedious computations [19, 11], the family of solutions in which we are interested is defined by

$$\mathbf{X}_{c_0}(s,t) = \sqrt{t}\mathbf{G}(s/\sqrt{t}), \tag{1.13}$$

where c_0 is the family parameter and $\mathbf{G}' = \mathbf{T}(s,1)$ is the solution of

$$\begin{pmatrix} \mathbf{T} \\ \mathbf{e}_1 \\ \mathbf{e}_2 \end{pmatrix}_s = \begin{pmatrix} 0 & c_0 & 0 \\ \mp c_0 & 0 & \frac{s}{2} \\ 0 & -\frac{s}{2} & 0 \end{pmatrix} \cdot \begin{pmatrix} \mathbf{T} \\ \mathbf{e}_1 \\ \mathbf{e}_2 \end{pmatrix}, \tag{1.14}$$

$\mathbf{T} \equiv \mathbf{X}_s$, $\mathbf{e}_1$ and $\mathbf{e}_2$ being the components of the generalized Frenet-Serret formulae; the initial conditions for (1.14) are

$$\begin{cases} \mathbf{G}(0) = 2c_0(0,1,0), \\ \mathbf{T}(0,1) = (0,0,1), \\ \mathbf{e}_1(0,1) = (1,0,0), \\ \mathbf{e}_2(0,1) = (0,1,0). \end{cases} \tag{1.15}$$

Finally, for $c_0 = 0$ we define

$$\mathbf{X}_0(s,t) = s(0,0,1). \tag{1.16}$$

It can be easily shown that, for an arbitrary $t > 0$, we have

$$\begin{pmatrix} \mathbf{T} \\ \mathbf{e}_1 \\ \mathbf{e}_2 \end{pmatrix}_s = \begin{pmatrix} 0 & \frac{c_0}{\sqrt{t}} & 0 \\ \mp\frac{c_0}{\sqrt{t}} & 0 & \frac{s}{2t} \\ 0 & -\frac{s}{2t} & 0 \end{pmatrix} \cdot \begin{pmatrix} \mathbf{T} \\ \mathbf{e}_1 \\ \mathbf{e}_2 \end{pmatrix}. \tag{1.17}$$

The one-parameter family of self-similar functions we have just defined satisfies the following theorem:

THEOREM 1.1. *Given $c_0 \geq 0$, the $\mathbf{X}_{c_0}$ defined by (1.13), (1.15) and (1.16) is a C^∞ solution of (1.8), $\forall t > 0$.*

Moreover, there are $\mathbf{A}^1(c_0)$, $\mathbf{A}^2(c_0)$, $\mathbf{B}^1(c_0)$, $\mathbf{B}^2(c_0)$ and a constant C such that
(i) $|\mathbf{X}_{c_0}(s,t) - \mathbf{A}^1 s(c_0)\chi_{[0,+\infty)}(s) - \mathbf{A}^2 s(c_0)\chi_{(-\infty,0]}(s)| \leq C\sqrt{t}.$

(ii) *We have the following asymptotics:*

$$\mathbf{G}(s) = \mathbf{A}^j(c_0)\left(s \pm 2\frac{c_0^2}{s}\right) - 4c_0\frac{\mathbf{e}_1}{s^2} + \mathcal{O}(1/s^3), \qquad s \to \pm\infty;$$

$$\mathbf{T}(s) = \mathbf{A}^j(c_0) - 2c_0\frac{\mathbf{e}_2}{s} + \mathcal{O}(1/s^2), \qquad s \to \pm\infty;$$

$$(\mathbf{e}_1 - i\mathbf{e}_2) = \mathbf{B}^j(c_0)e^{is^2/4}e^{\pm ic_0^2 \log|s|} + \mathcal{O}(1/s), \qquad s \to \pm\infty;$$

where the superindex $j = 1$ when $s \to \infty$ and $j = 2$ when $s \to -\infty$.
(iii) $\mathbf{A}^j = (A_1^j, A_2^j, A_3^j)$ *and* $\mathbf{B}^j = (B_1^j, B_2^j, B_3^j)$ *are vectors, with* $\mathbf{A}^j \circ_\pm \mathbf{A}^j = \pm 1$
and

$$A_1^1 = -A_1^2, \qquad A_2^1 = -A_2^2, \qquad A_3^1 = A_3^2 = e^{\mp\frac{c_0^2}{2}\pi},$$
$$B_1^1 = B_1^2, \qquad B_2^1 = B_2^2, \qquad B_3^1 = -B_3^2, \qquad \mathbf{A}^j \circ_\pm \mathbf{B}^j = 0,$$

We have combined in this theorem the results for both the Euclidean and the Hyperbolic cases, proved in [19] and [11], respectively. Naturally, $\mathbf{A}^j$, $\mathbf{B}^j$ and C are different in each case.

It follows from this theorem that there exists a solution to (1.8) such that

$$\mathbf{X}(s,0) = \mathbf{A}^1 s\chi_{[0,+\infty)}(s) + \mathbf{A}^2 s\chi_{(-\infty,0]}(s), \tag{1.18}$$

and, correspondingly for (1.9),

$$\mathbf{T}(s,0) = \mathbf{A}^1 \chi_{[0,+\infty)}(s) + \mathbf{A}^2 \chi_{(-\infty,0]}(s). \tag{1.19}$$

Observe that both (1.8) and (1.9) are time reversible, because if $\mathbf{X}(s,t)$ and $\mathbf{T}(s,t)$ are their respective solutions, so are $\mathbf{X}(-s,-t)$ and $-\mathbf{T}(-s,-t)$. Therefore, we have two
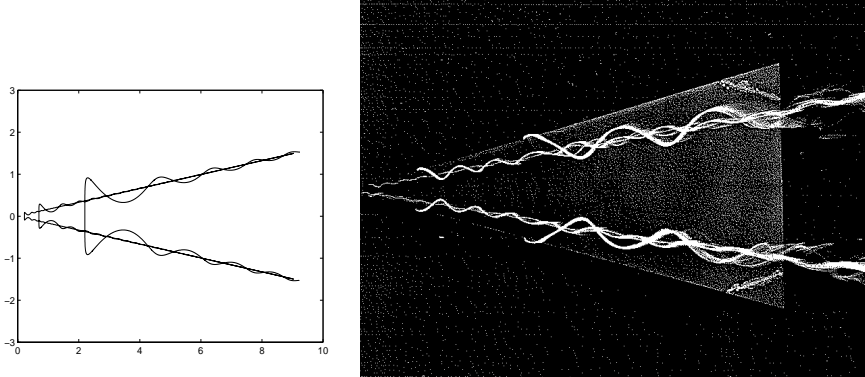

FIG. 1.1. *Comparison between the theoretical evolution of* $\mathbf{X}(s,t)$ *and a real experiment of a colored fluid traversing a triangular wing. The experimental result on the right has been taken from [29].*

one-parameter families of regular solutions that develop singularities at finite time. In the case of $\mathbf{X}$, we have precisely a corner-shaped singularity, having thus a good model to describe some natural phenomena. In Figure 1.1, for instance, we have plotted on the left hand-side the evolution of $\mathbf{X}(s,t)$, obtained by integrating (1.17), and on the right hand side, a picture of an experiment published in ONERA [29], where several

lines of colored fluid in water show the symmetrical pair of vortices behind an inclined delta wing, with a high Reynolds number. The resemblance between both images is really striking, at least at the qualitative level. In fact, in both images we clearly see the self-similar behavior of the evolution of the filaments. Also in both cases the filaments tend asymptotically to two non-parallel lines. Finally, both pictures have in common the oscillatory behavior, and the shift of the horse-shoe-type of curve that is close to the vertex with respect to the plane that contains the two asymptotic lines. See also figures 7.5.7 and 7.8.6 of plate 2 in [5]. It would be interesting to know if this resemblance is not just at the qualitative level. Notice that Theorem 1.1 quantifies in a precise manner the above mentioned properties for the self-similar solutions of the LIA.

The main difference between the Euclidean and the hyperbolic case is the fact that

$$A_3^1 = A_3^2 = e^{\mp \frac{c_0^2}{2}\pi}, \tag{1.20}$$

i.e., A_3^j grow exponentially with c_0 in the hyperbolic case. Thus, although $\mathbf{T}$, $\mathbf{e}_1$ and
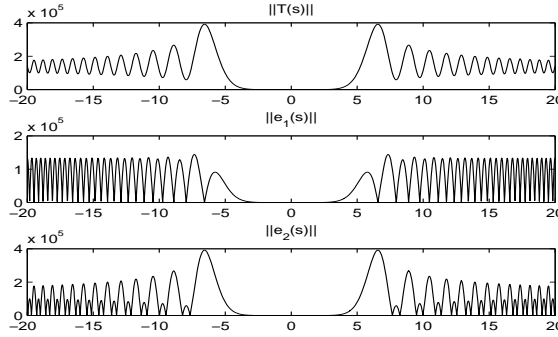

FIG. 1.2. $c_0 = 2.7$, hyperbolic case. Euclidean lengths of $\mathbf{T}$, $\mathbf{e}_1$ and $\mathbf{e}_2$

$\mathbf{e}_2$ are also bounded in the hyperbolic case for a given c_0, this is by no means trivial, unlike in the Euclidean case; moreover, there are no global bounds valid for all c_0 and the bounds grow very fast even for relatively small values of c_0. In Figure 1.2, for instance, we have plotted the Euclidean lengths of $\mathbf{T}$, $\mathbf{e}_1$ and $\mathbf{e}_2$ in the hyperbolic case, for $c_0 = 2.7$; the lengths are seen to be $\mathcal{O}(10^5)$. This fact makes the proof of Theorem 1.1 much more difficult in the Hyperbolic case, as well as the numerical treatment of (1.8) and (1.9) for large values of c_0.

Now, (1.8) is invariant under translations and also under rotations in the Euclidean case and under Lorentz transformations with unitarian determinant in the hyperbolic case; hence, given two arbitrary $\mathbf{A}^j$ in $\mathbb{S}^2$ or $\mathbb{H}^2$, we can transform (1.8), so that $\mathbf{A}^j$ have the form as in part (iii) of Theorem 1.1. Then, it is possible to obtain the corresponding c_0. Observe that for all $\mathbf{A}^j \in \mathbb{H}^2$ there is a corresponding c_0. However, when $\mathbf{A}^1 = \mathbf{A}^2 \in \mathbb{S}^2$, which can be reduced to $\mathbf{A}^1 = \mathbf{A}^2 = (0,0,1)$, c_0 should be infinity, so there is no real c_0 matching that case.

There is a natural connection between equations (1.8) and (1.9), and the nonlinear Schrödinger equation. Equation (1.8) can be transformed into the Schrödinger equation with a cubic nonlinearity via a transformation introduced by Hasimoto [20].

Especifically, define

$$\psi(s,t) = c(s,t) \exp\left(i \int_0^s \tau(s',t')\, ds'\right). \tag{1.21}$$

Then, ψ satisfies the equation

$$i\psi_t + \psi_{ss} \pm \frac{1}{2}\left(|\psi|^2 + A(t)\right)\psi = 0, \tag{1.22}$$

for some function $A(t)$, which can be removed by means of an integrating factor.

Equation (1.9) can be transformed into a nonlinear Schrödinger equation by performing a stereographic projection onto the complex plane. If we define

$$z(s,t) = \frac{T_1}{1+T_3} + i\frac{T_2}{1+T_3}, \tag{1.23}$$

then z satisfies the equation [28]

$$z_t = iz_{ss} \mp \frac{2i\bar{z}}{1 \pm |z|^2}z_s^2. \tag{1.24}$$

In this article, we study the self-similar solutions described above from a numerical point of view, in order to understand the singularity formation, as well as the mechanism for energy concentration that is responsible for the formation of such singularity. These solutions can be studied at the level of $\mathbf{X}$ (eq. (1.8)), $\mathbf{T}$ (eq. (1.9)), ψ (eq. (1.22)), or at the level of z (eq. (1.24)). However, we will not work directly with (1.8), given that $\mathbf{X}$ can be recovered from $\mathbb{R}$ except for a constant of integration that is fixed by considering (1.13), i.e.,

$$\mathbf{X}(s,0) = 2c_0\sqrt{t}(0,1,0). \tag{1.25}$$

Although there is a rich literature concerning the numerical study of (1.4) and, in general, the Landau-Lifshitz equation (see, for instance, [9, 16, 17, 13]), the materials analyzing the numerics of the self-similar solutions we are considering are very scarce; the most relevant results were given by Buttke some twenty years ago [7]. Nevertheless, Buttke only considered the forward case, starting with a singular initial datum at $t = 0$ and going forward in time; we are interested in the singularity formation process, and therefore will focus mostly in the backward case, i.e., starting from $t = 1$, we will approach the singularity time.

Moreover, we are not aware of any other study of the hyperbolic case. For small c_0, the results of both cases are virtually identical; because of that, we have used in our experiments $c_0 = 0.2$. In contrast, for bigger c_0, because of the rapid growth of the Euclidean lengths of $\mathbf{T}$, $\mathbf{e}_1$ and $\mathbf{e}_2$ (see Figure 1.2), the hyperbolic case becomes much more difficult to treat numerically, requiring a finer study, which we postpone for the future.

The three equations (1.9), (1.22), and (1.24) are posed in the whole real line. To carry out the numerical simulations, we must restrict ourselves to an interval $[-L, L]$ (for L large enough). It is important then to give appropriate boundary conditions in order to capture the singularity formation mechanism. In [7], only periodic boundary conditions were considered.

The experiments performed here constitute numerical evidence of the stability of (1.8), (1.9) and (1.24), and in particular of the robustness of the energy concentration

mechanism. Indeed, one can never introduce numerically completely exact boundary conditions at $s = \pm L$; in the best of the cases, there will be small errors due to machine precision and in the worst one, we will be using very rough boundary conditions. Therefore, we can consider that we are computing perturbed versions of the exact solutions. In a recent series of articles [3, 4] Banica and Vega prove the stability of the solutions that we consider at the level of $\mathbf{T}$. At the level of ψ, Banica and Vega [4] also prove that a logarithmic instability appears when t comes close to zero. Notice that $\mathbf{T}$ involves one integral with respect to the curvature and two with respect to the torsion. In our case these are highly oscillatory integrals so that, due to the cancelations, $\mathbf{T}$ and $\mathbf{X}$ become stable. These results give the theoretical basis to the numerical results presented here, and suggest that it is better to work numerically with the equations at the level of $\mathbf{T}$ or $\mathbf{z}$. Therefore, we consider only equations (1.9), and (1.24).

We return now to the issue of boundary conditions. For equation (1.9), we consider two types of boundary conditions, derived from the asymptotics of $\mathbf{T}$ given in Theorem 1.1. The first boundary condition is simply $\mathbf{T}(\pm L, t) = \mathbf{T}(\pm, 1)$ and for the second one, we keep the first-order term in the asymptotics of $\mathbf{T}(s, 1)$ and use the fact that $\mathbf{T}(s, t) = \mathbf{T}(s/\sqrt{t}, 1)$.

For equation (1.24), we consider three types of boundary conditions: the first one is the projected boundary condition used for $\mathbf{T}$, The second boundary condition is derived from the self-similarity condition, i.e., $z(s, t) = z(s/\sqrt{t}, 1)$. Unlike the former one, this condition is not an approximate one, so it introduces no noise, giving very clean results. Finally, we derive a radiation boundary condition. This condition seems to perform best, and in contrast to the previous two conditions, can be used in the progressive case.

The remainder of the article is organized as follows: Equation (1.9) is considered in section 2, where we use a simple spatial discretization using finite differences. The nonlinearity in the equation and the constraint $\mathbf{T}=1$, make it difficult to construct efficient implicit methods for these equations [16]. For the two boundary conditions mentioned earlier, we observe an stability constraint of $|\Delta t| = \mathcal{O}(\Delta s^2)$. The first condition only reproduces the singularity formation from a qualitative point of view, while the second one gives good results for all s, even for very small t, although a very small Δs may be needed.

In section 3, we consider equation (1.24). This equation adapts well to a pseudo-spectral method using Chebyshev polynomials; comprehensive information about this family of polynomials can be found, for instance, in [14] and [18]. We use also a Chebyshev point distribution, which is now much better suited, since a denser concentration of points is required near the boundary for small t and, specially, for big L, which is when the pseudo-spectral method really excels.

In order to measure the accuracy of our results, we compute the error in the curvature obtained from $\mathbf{T}$ (which, when necessary, can be recovered from z as well), since the correct curvature has the known value $c(s, t) = \frac{c_0}{\sqrt{t}}$.

Finally, the stability results of Banica and Vega are described in section 4.

2. Schrödinger map. We consider equation

$$\begin{cases} \mathbf{T}_t(s, t) = \mathbf{T}(s, t) \wedge_{\pm} \mathbf{T}_{ss}(s, t), & s \in [-L, +L] \\ \mathbf{T}(s, 1) = \mathbf{T}^0(s). \end{cases} \tag{2.1}$$

In his Ph. D. Thesis, Buttke considered the following Crank-Nicholson type numerical scheme to integrate the Euclidean version of (2.1) [6]:

$$\frac{\mathbf{T}(s, t + \Delta t) - \mathbf{T}(s, t)}{\Delta t} = \frac{\mathbf{T}(s, t + \Delta t) + \mathbf{T}(s, t)}{2} \wedge \left(\frac{D_{+-}\mathbf{T}(s, t + \Delta t) + D_{+-}\mathbf{T}(s, t)}{2} \right),$$
$$(2.2)$$

where D_{+-} represents the approximation to the second derivative using standard centered differences, i.e.,

$$D_{+-}T(s, t) = \frac{T(s + \Delta s, t) - 2T(s, t) + T(s - \Delta s, t)}{\Delta s^2}. \qquad (2.3)$$

Buttke only studied the forward case, i.e., starting from $t = 0$ and, concentrating all the information of $\mathbf{T}$ at $s = 0$, he tried to recover the self-similar solutions we have described above, by imposing periodic boundary conditions at $\pm L$.

The scheme used by Buttke's is implicit, and he used a fixed-point iteration method to advance to the next time step. For this iteration to converge, a time step $\Delta t = \mathcal{O}(\Delta s^2)$ is needed. Therefore, although the method is a priori unconditionally stable, in practice it is not.

We have observed that an explicit finite difference scheme is equally efficient; more precisely, a scheme using a second-order finite difference scheme in space with the classical fourth order Runge-Kutta in time works well. In what follows, we have considered the backward case, starting at $t = 1$ and trying to arrive at $t = 0$.

We divide $[-L, +L]$ in N equally spaced parts, $-L = s_0 < s_1 < \cdots < s_{N-1} < s_N = +L$, with

$$s_i = -L + i\Delta s, \qquad \Delta s = \frac{2L}{N}, \qquad i = 0, \cdots, N.$$

Equation (1.9) is discretized as

$$\mathbf{T}_t(s, t) = \mathbf{T}(s, t) \wedge_\pm D_{+-}T(s, t),$$

and the time-stepping is carried out with the classical fourth order Runge-Kutta. By using a fourth order Runge-Kutta, we guarantee that $\mathbf{T} \circ_\pm \mathbf{T} = \pm 1$ is preserved with high accuracy. Nevertheless, we normalize $\mathbf{T}$ at every time step by doing

$$\mathbf{T}_i^{n+1} \equiv \frac{\mathbf{T}_i^{n+1}}{(\pm\mathbf{T}_i^{n+1} \circ_\pm \mathbf{T}^{n+1})^{\frac{1}{2}}}. \qquad (2.4)$$

A higher order finite difference scheme could be effortlessly implemented, although we have observed that this does not improve significantly the quality of our results.

Experimentally, $|\Delta t| \lesssim 0.7\Delta s^2$ is found to be needed for the method to be stable. Thus, as in Buttke's method, we have a $\Delta t = \mathcal{O}(\Delta s^2)$ restriction, but it is straightforward to advance to the next time step.

From theorem 1.1, we know that the self-similar solution $\mathbf{T}^0$ has the following asymptotic expansion:

$$\mathbf{T}^0(s) = \mathbf{A}^j(c_0) - 2c_0 \frac{\mathbf{e}_2}{s} + \mathcal{O}(1/s^2). \qquad (2.5)$$

We approximate the boundary conditions for (1.9) by the values of $T^0(s/\sqrt{t})$, and consider two types of boundary conditions:

1. First order boundary conditions:

$$T(+L, t) = A^+,$$
$$T(-L, t) = A^-. \tag{2.6}$$

2. Second order boundary conditions:

$$T(+L, t) = A^+ - 2c_0\sqrt{t}\frac{\mathbf{e}_2(+L/\sqrt{t})}{L},$$
$$T(-L, t) = A^- + 2c_0\sqrt{t}\frac{\mathbf{e}_2(-L/\sqrt{t})}{L}, \tag{2.7}$$

normalized to be of length 1. In (2.7), we use the leading order in the asymptotics for $\mathbf{e}_2$, obtained from theorem 1.1 on page 1.1 as well.

2.1. First order boundary conditions. We set

$$T(+L, t) = A^+,$$
$$T(-L, t) = A^-, \quad \forall t, \tag{2.8}$$

and obtain the initial datum $\mathbf{T}(s, 1)$ by integrating (1.14) for $s \in [-L, L]$, using (1.15) as initial condition. We have also used a fourth order Runge-Kutta, normalizing every $\mathbf{T}^n \equiv \mathbf{T}(s_n, 1)$, $\mathbf{e}_1^n \equiv \mathbf{e}_1(s_n, 1)$ and $\mathbf{e}_2^n \equiv \mathbf{e}_2(s_n, 1)$:

$$\mathbf{T}^{n+1} \equiv \frac{\mathbf{T}^{n+1}}{(\pm\mathbf{T}^{n+1} \circ_\pm \mathbf{T}^{n+1})^{\frac{1}{2}}}, \quad \mathbf{e}_1^{n+1} \equiv \frac{\mathbf{e}_1^{n+1}}{(\mathbf{e}_1^{n+1} \circ_\pm \mathbf{e}_1^{n+1})^{\frac{1}{2}}}, \quad \mathbf{e}_2^{n+1} \equiv \frac{\mathbf{e}_2^{n+1}}{(\pm\mathbf{e}_2^{n+1} \circ_\pm \mathbf{e}_2^{n+1})^{\frac{1}{2}}}. \tag{2.9}$$

We have executed our method $c_0 = 0.2$ and different value for L. In our experiments, we have chosen $|\Delta t| = 0.5\Delta s^2$. Smaller $|\Delta t|$ do not improve the results, since the method is fourth-order accurate in time. With fixed boundary conditions, the choice of Δs is also not very important; in what follows, we show the results for $L = 10$ and $L = 50$, having used $\Delta s = 0.01$, $\Delta t = -5 \cdot 10^{-5}$. With these parameters, we have seen that smaller Δs produce virtually identical results. Nevertheless, for bigger L, it is convenient to use smaller Δs.

To measure the quality of the results at a given t, we analyze the curvature $c = \sqrt{\mathbf{T}_s \circ_\pm \mathbf{T}_s}$.

In Figure 2.1 we show the curvature as a function of s and t, for $L = 10$ and $L = 50$. The accuracy is lost as we approach $t = 0$, although as one would expect, the bigger L is, the better the results are. However, it is remarkable the good accuracy with which one recovers the curvature at $s = 0$, even for small times, as we can see in Figure 2.2. Again, this accuracy improves as we increase L. Finally, it is also remarkable the fact that the energy between $[-L, L]$,

$$\int_{-L}^{+L} c^2(s, t)ds, \tag{2.10}$$

calculated with the trapezoidal rule, is preserved with several precision digits (see Figure 2.3). This is approximately $2Lc_0^2$ for all t. Since the curvature at $s = 0$ is quite well recovered and the energy well preserved, we are able to reproduce the behavior
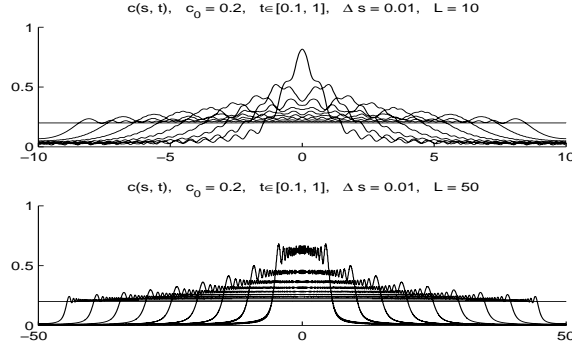
FIG. 2.1. *Curvature at* $t \in \{1, 0.9, \cdots, 0.1\}$, *with* $\Delta s = 0.01$, $L = 10, 50$. *Although the results for* $L = 10$ *are very poor, for* $L = 50$ *we notice a remarkable improvement.*
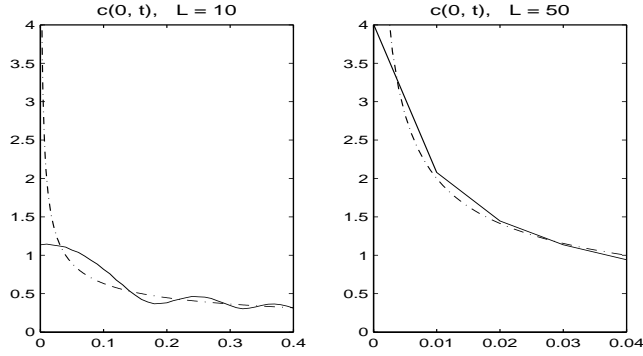

FIG. 2.2. *Curvature at* $s = 0$, *with* $\Delta s = 0.01$, $L = 10, 50$, *together with its theoretical value. The accuracy improves notably when increasing* L.
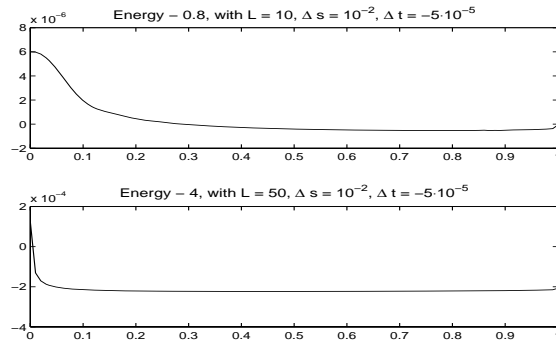

FIG. 2.3. *Error in the conservation of the energy, for* $L = 10$ *and* $L = 50$, *using finite differences and fixed extremes. Although the method is not symplectic, it preserves the energy very well.*

of $\mathbf{T}$ correctly, at least from a qualitative point of view. Indeed, in the exact solution,

the energy in $(-\infty, \infty)$ is preserved:

$$\int_{-\infty}^{+\infty} c^2(s,t)ds = \infty, \qquad \forall t; \tag{2.11}$$

this infinite energy tends to concentrate at $s = 0$, which causes the singularity to be produced. Now, we are working at $[-L, L]$, but the finite energy is also preserved and it also tends to concentrate on $s = 0$, so we can approximate the formation of the singularity at $t = 0$. Moreover, by increasing L, we are able to recover $c(0,t)$ for smaller times, improving the quality of the results.

2.2. Second order boundary conditions. We set now

$$\mathbf{T}(+L,t) = \mathbf{A}^+ - 2c_0\sqrt{t}\frac{\mathbf{e}_2(L,t)}{L} = \mathbf{A}^+ + 2c_0\sqrt{t}\frac{\Im[\mathbf{B}^+e^{iL^2/4t}]}{L}, \tag{2.12}$$

$$\mathbf{T}(-L,t) = \mathbf{A}^- + 2c_0\sqrt{t}\frac{\mathbf{e}_2(-L,t)}{L} = \mathbf{A}^- - 2c_0\sqrt{t}\frac{\Im[\mathbf{B}^-e^{iL^2/4t}]}{L}, \tag{2.13}$$

normalized to be of length 1.

Using these asymptotics as the boundary condition allows us to obtain solutions that are not only qualitatively, but also quantitatively correct. The reason for this is that the new boundary conditions allow us to introduce energy into the system, as time evolves, which concentrates in order to form a cusp at the origin $s = 0$.

Here, the choice of Δs is much more delicate. For small t and, specially, for big L, we have problems of aliasing, since the boundary conditions (2.12) are highly oscillatory. In Figure 2.4, we show the curvature at several instants in time, obtained using $\Delta s = 0.01$, $\Delta s = -5 \cdot 10^{-5}$ and $L = 10$ and $L = 50$. At $t = 0.1$, the curvature has completely degraded for $L = 50$.
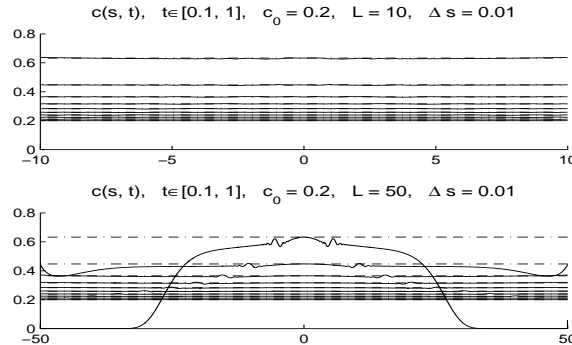

FIG. 2.4. *Curvature in $t \in \{1, 0.9, \cdots, 0.1\}$, con $\Delta s = 0.01$ y $L \in \{10, 50\}$. The results tend to worsen when increasing L.*

2.3. Progressive case. In the progressive case, considered by Buttke in his Ph. D. thesis [6], we start at $t = 0$ and go forward in time, trying to recover the self-similar solutions. Hence, we want to solve numerically the following initial value problem

$$\begin{cases} \mathbf{T}_t(s,t) = \mathbf{T}(s,t) \wedge_\pm \mathbf{T}_{ss}(s,t), & s \in (-\infty, +\infty), \\ \mathbf{T}(s,0) = \mathbf{A}^1\chi_{[0,+\infty)}(s) + \mathbf{A}^2\chi_{(-\infty,0]}(s). \end{cases} \tag{2.14}$$

Again, since we cannot consider the whole $\mathbb{R}$, we study

$$\begin{cases} \mathbf{T}_t(s,t) = \mathbf{T}(s,t) \wedge_{\pm} \mathbf{T}_{ss}(s,t), & s \in [-L,+L], \\ \mathbf{T}(s,0) = \mathbf{A}^1 \chi_{[0,+\infty)}(s) + \mathbf{A}^2 \chi_{(-\infty,0]}(s). \end{cases} \tag{2.15}$$

We impose the boundary conditions $\mathbf{T}(+L,t) = \mathbf{T}(+L,0) = \mathbf{A}^1$ and $\mathbf{T}(-L,t) = \mathbf{T}(-L,0) = \mathbf{A}^2$. Dividing $[-L,L]$ in N parts of the same length, our initial datum will be

$$\begin{cases} \mathbf{T}_i^0 = \mathbf{A}^2, & i = 0, \cdots, \dfrac{N}{2} - 1, \\ \mathbf{T}_i^0 = (0,0,1), & i = \dfrac{N}{2}, \\ \mathbf{T}_i^0 = \mathbf{A}^1, & i = \dfrac{N}{2} + 1, \cdots, N, \end{cases} \tag{2.16}$$

where $\mathbf{T}_i^0 \equiv \mathbf{T}(s_i, t^0) = \mathbf{T}(s_i, 0)$, $s_i = -L + i\dfrac{2L}{N}$ and $\mathbf{T}(0,0) = (0,0,1)$, in order to be consistent with the backward case. Because of symmetries, $\mathbf{T}(0,t) = (0,0,1)$, $\forall t > 0$. Because of part (iii) of Theorem 1.1, $(\mathbf{A}^1)_3 = (\mathbf{A}^2)_3 = e^{\mp \frac{c_0^2}{2}\pi}$. Therefore, once c_0 is fixed, we can chose some adequate $\mathbf{A}^1$ and $\mathbf{A}^2$:

$$\mathbf{A}^1 = \left(\sqrt{\pm(1 - e^{\mp c_0^2 \pi})}, 0, e^{\mp \frac{c_0^2}{2}\pi} \right), \quad \mathbf{A}^2 = \left(-\sqrt{\pm(1 - e^{\mp c_0^2 \pi})}, 0, e^{\mp \frac{c_0^2}{2}\pi} \right). \tag{2.17}$$

If we executed the backward case with that c_0, we would obtain those $\mathbf{A}^1$ and $\mathbf{A}^2$, except for a rotation around the z axis, which numerically has no relevance.

In Figure 2.5, we have taken $L = 50$, $10000+1$ points, i.e., $\Delta s = 0.01$; $\Delta t = 5\cdot 10^{-5}$ and $c_0 = 0.2$. We have drawn the curvature between $t = 0.025$ and $t = 0.25$, with increments of 0.025. It is clear that the information goes outwards with constant velocity. The correct theoretical curvature is shown with discontinuous strokes. We can appreciate that the accuracy of the results improves with time.
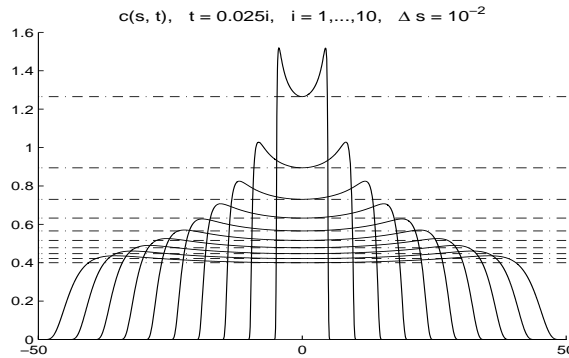

FIG. 2.5. *Curvature for different t. Progressive case with finite differences. We observe that the exactitude of the results improves with time; the best result is obtained at $t = 0.25$.*

Thus, if we want to recover the curve for a given interval at a given time, we have to consider a Δs small enough and a $[-L, L]$ big enough.

If, however, we fix the boundary conditions, once the information has reached the boundary, it is reflected back into the domain, causing the appearance of fractal-like phenomena. In figure, 2.6, we have drawn the two cases of $\mathbf{T}$, for $c_0 = 0.2$, $s \in [-50, 50]$, $\Delta s = 0.1$, $\Delta t = 5 \cdot 10^{-5}$, $t = 10$. Although the approximated boundary

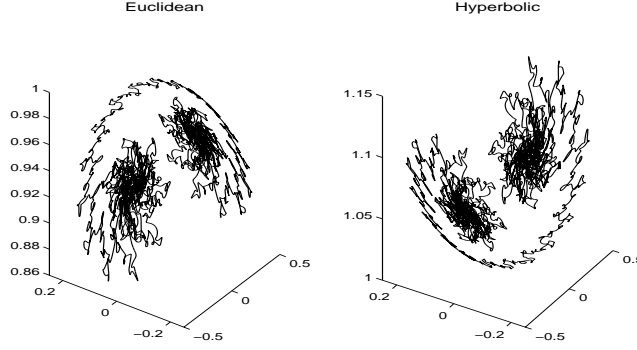FIG. 2.6. *Fractal formation in* $\mathbf{T}$

condition is convenient for the backward case, it does not seem to be appropriate for the forward case, as we can see in Figure 2.7. We will get back to this issue in section
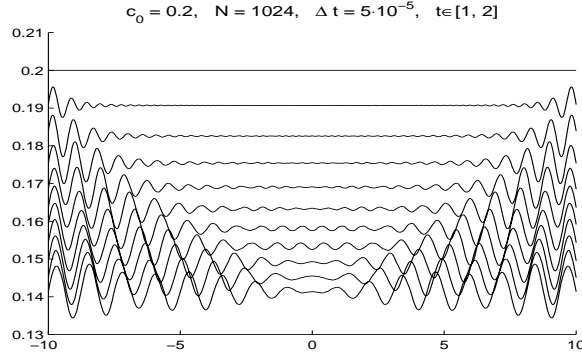

FIG. 2.7. *Progressive case, starting from $t = 1$, till $t = 2$. As we see, the approximated boundary condition is not adequate for the forward case.*

3, where we consider a spectral discretization of (1.24).

Finally, let us mention that the finite difference models have another problem in the forward model, which Buttke also observed. Indeed, the curvature error grows severely as we make $\Delta t \to 0$ (see Figure 2.8). In Section 3, this will also be solved.

2.4. Evolution of X. Once $\mathbf{T}(s, t)$ has being calculated, it is immediate to recover $\mathbf{X}(s, t)$, since

$$\begin{cases} \mathbf{X}_s(s, t) = \mathbf{T}(s, t) \\ \mathbf{X}(0, t) = 2c_0\sqrt{t}(0, 1, 0); \end{cases} \tag{2.18}$$
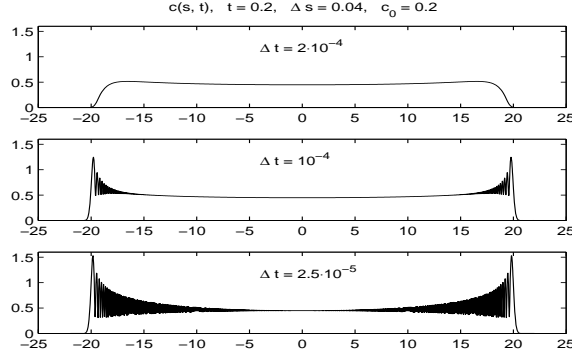
FIG. 2.8. *Curvature noise when decreasing Δt*

We integrate this equation using the scheme

$$\mathbf{X}^{n+1} = \mathbf{X}^n + \frac{\Delta s}{24}(9\mathbf{T}^n + 19\mathbf{T}^{n+1} - 5\mathbf{T}^{n+2} + \mathbf{T}^{n+3}), \qquad (2.19)$$
$$s_{n+1} = s_n + \Delta s,$$

which, in principle, is fourth order accurate in Δs. Note, however, that $\mathbf{T}$ is only obtained to second order accuracy in Δs, resulting overall in a second order method. However, we use the fourth order scheme in order to reduce the accumulation of errors.
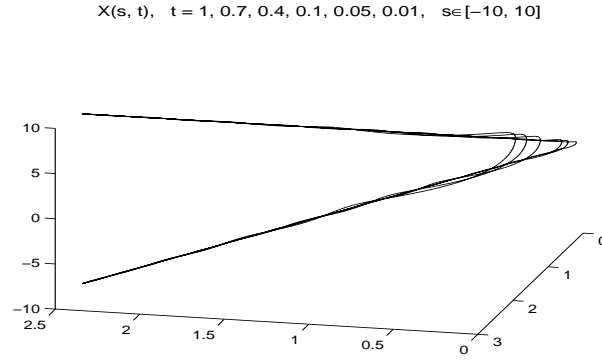
FIG. 2.9. *Corner formation for* $\mathbf{X}$. *Fixed extremes.*

We have recovered $\mathbf{X}$ for both boundary conditions. In Figure 2.9, we have obtained $\mathbf{T}$ with fixed extremes and the parameters of the experiment corresponding to the second graphic in Figure 2.1, i.e., Euclidean case, $c_0 = 0.2$, $L = 50$, $\Delta s = 0.01$, $\Delta t = -5 \cdot 10^{-5}$, drawing only $s \in [-10, 10]$.

In Figure 2.11, we have drawn the $\mathbf{X}$ recovered from $\mathbf{T}$, with the parameters of the experiment corresponding to Figure 2.10. For this experiment, we had used the second order boundary condition, so we can see the corner formation with much greater clarity. Except for this, the two figures are rather similar.

$c(s, t), \quad t \in [0.003, 0.015], \quad c_0 = 0.2, \quad L = 10, \quad \Delta s = 5 \cdot 10^{-4}$
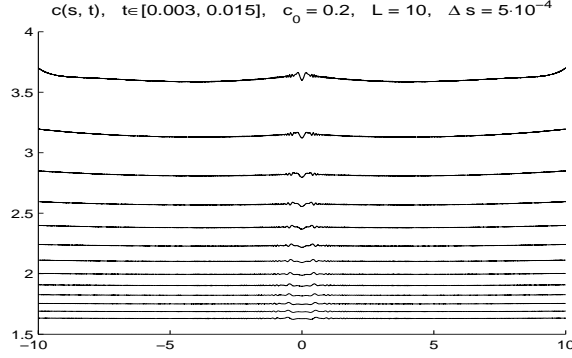
FIG. 2.10. *Curvature at* $t \in \{0.003, 0.004, \cdots, 0.015\}$, *with* $\Delta s = 5 \cdot 10^{-4}$.

$X(s, t), \quad t = 1, 0.5, 0.1, 0.05, 0.003$
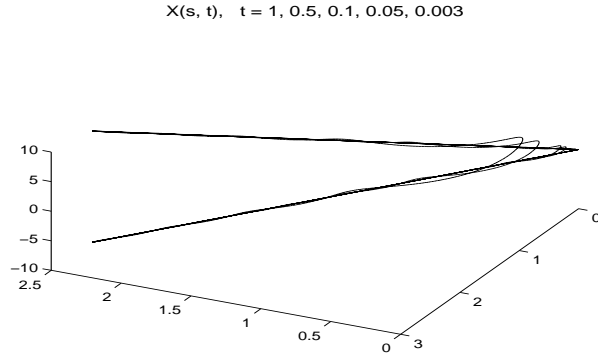
FIG. 2.11. *Corner formation for* **X**. *Approximated boundary.*

3. Schrödinger map: Stereographic projection.

We consider now the stereographic projection of $\mathbf{T} = (T_1, T_2, T_3)$ over $\mathbb{C}$:

$$z = x + iy \equiv (x, y) \equiv \left(\frac{T_1}{1 + T_3}, \frac{T_2}{1 + T_3} \right). \tag{3.1}$$

We are projecting $\mathbf{T}$ from $(0, 0, -1)$ into $\mathbb{R}^2$, identifying $\mathbb{R}^2$ with $\mathbb{C}$. In the Euclidean case, where $\mathbf{T} \in \mathbb{S}^2$, there is a point on the sphere, $(0, 0, -1)$, to which no point in $\mathbb{C}$ corresponds, because the sphere is compact. Thus, we have a bijection between $\mathbb{S}^2 - \{(0, 0, -1)\}$ and $\mathbb{R}^2$. In the hyperbolic case, when $\mathbf{T} \in \mathbb{H}^2$, since $T_3 > 0$, we have a bijection between $\mathbb{D}$ and $\mathbb{H}^2$, where

$$\mathbb{D} = \{(x, y) \in \mathbb{R}^2 \ / \ x^2 + y^2 < 1\}$$

is commonly referred to as the Poincaré disc. Unlike in the Euclidean case, we do not need to eliminate any point from $\mathbb{H}^2$. The tangent vector $\mathbf{T}$ can be recovered from z by the inverse map:

$$\mathbf{T} = (T_1, T_2, T_3) \equiv \left(\frac{2x}{1 \pm x^2 \pm y^2}, \frac{2y}{1 \pm x^2 \pm y^2}, \frac{1 \mp x^2 \mp y^2}{1 \pm x^2 \pm y^2} \right). \tag{3.2}$$

Now, differentiating z in (3.1), together with (1.9) and (3.2), we get the following nonintegrable, nonlinear Schrödinger equation for z:

$$z_t = iz_{ss} \mp \frac{2i\bar{z}}{1 \pm |z|^2} z_s^2. \tag{3.3}$$

The advantage of this equation, as opposed to (1.8) and (1.9), is that the higher order term z_{ss} treated implicitly, eliminating, or at least reducing significantly the restrictions for Δt.

We can also express the other elements of the generalized Frenet-Serret formulae (1.11), i.e., c, τ, $\mathbf{e}_1$ and $\mathbf{e}_2$ in terms of z. We get the generalized curvature from $c = (\mathbf{T}_s \circ_{\pm} \mathbf{T}_s)^{1/2}$:

$$c = (T_{1s}^2 + T_{2s}^2 \pm T_{3s}^2)^{\frac{1}{2}} = \frac{2(x_s^2 + y_s^2)^{\frac{1}{2}}}{1 \pm x^2 \pm y^2} = \frac{2|z_s|}{1 \pm |z|^2}. \tag{3.4}$$

The expression for the generalized torsion is somewhat more involved:

$$\begin{aligned} \tau &= \frac{1}{c^2} \mathbf{T} \circ_{\pm} (\mathbf{T}_s \wedge_{\pm} \mathbf{T}_{ss}) \\ &= \frac{2\Im(z\bar{z}_s)}{|z|^2 \pm 1} + \frac{\Im(\bar{z}_s z_{ss})}{|z_s|^2}. \end{aligned} \tag{3.5}$$

The expression for $\mathbf{e}_1$ follows from $\mathbf{e}_1 = \frac{1}{c}\mathbf{T}_s$:

$$\mathbf{e}_1 = \frac{1}{(x_s^2 + y_s^2)^{\frac{1}{2}}} \left(\frac{x_s(1 \mp x^2 \pm y^2) \mp 2xyy_s}{1 \pm x^2 \pm y^2}, \frac{y_s(1 \pm x^2 \mp y^2) \mp 2xyx_s}{1 \pm x^2 \pm y^2}, \frac{\mp 2xx_s \mp 2yy_s}{1 \pm x^2 \pm y^2} \right). \tag{3.6}$$

Finally, we obtain $\mathbf{e}_2$ from $\mathbf{e}_2 = \mathbf{T} \wedge_{\pm} \mathbf{e}_1$:

$$\mathbf{e}_2 = \frac{1}{(x_s^2 + y_s^2)^{1/2}} \left(\frac{\mp 2xx_s y - y_s(1 \mp x^2 \pm y^2)}{1 \pm x^2 \pm y^2}, \frac{\pm 2xyy_s + x_s(1 \pm x^2 \mp y^2)}{1 \pm x^2 \pm y^2}, \frac{\pm 2xy_s \mp 2x_s y}{1 \pm x^2 \pm y^2} \right). \tag{3.7}$$

3.1. Self-similar solutions. The self-similar solutions of $\mathbf{T}$ correspond to self-similar solutions of

$$z_t = iz_{ss} \mp \frac{2i\bar{z}}{1 \pm |z|^2} z_s^2. \tag{3.8}$$

To obtain them, note that if z is a solution of (3.8), so is $z_\lambda(s,t) = z(\lambda s, \lambda^2 t)$, for all λ. Taking $\lambda = t^{-1/2}$,

$$z(s,t) = z(s/\sqrt{t}, 1) = f(s/\sqrt{t}),$$

where $f(s) \equiv z(s,1)$. Introducing $f(s/\sqrt{t})$ in (3.8),

$$-\frac{1}{2} st^{-3/2} f'(s/\sqrt{t}) = \frac{i}{t} f''(s/\sqrt{t}) \mp \frac{2i\bar{f}(s/\sqrt{t})}{1 \pm |f(s/\sqrt{t})|^2} \frac{1}{t} (f'(s/\sqrt{t}))^2.$$

Setting $t = 1$,

$$-\frac{1}{2} sf'(s) = if''(s) \mp \frac{2i\bar{f}(s)}{1 \pm |f(s)|^2} (f'(s))^2;$$

hence

$$f''(s) = \frac{is}{2}f'(s) \pm \frac{2\bar{f}(s)}{1 \pm |f(s)|^2}(f'(s))^2. \tag{3.9}$$

Using the same initial conditions as before, $\mathbf{T}(0,1) = (0,0,1)$ and $\mathbf{T}_s(0,1) = c_0(1,0,0)$, we get

$$\begin{cases} f(0) = z(0,1) = 0, \\ f'(0) = z_s(0,1) = \dfrac{c_0}{2}. \end{cases} \tag{3.10}$$

It is immediate to generalize these expressions for times other than $t = 1$. Defining $g(s) = f(s/\sqrt{t}) = z(s,t)$, the EDO for $g(s)$ is

$$\begin{cases} g''(s) = i\dfrac{s}{2t}g'(s) \pm \dfrac{2\bar{g}(s)}{1 \pm |g(s)|^2}(g'(s))^2 \\ g(0) = f(0) = 0 \\ g'(0) = \dfrac{1}{\sqrt{t}}f'(0) = \frac{c_0}{2\sqrt{t}}. \end{cases} \tag{3.11}$$

Integrating (3.9), or eventually (3.11), we get the initial datum for (3.8). We use a fourth-order Runge-Kutta method to integrate (3.11). We obtain $f(s)$ for $s \geq 0$. The values $f(s)$ for $s < 0$ are obtained by symmetry, since $f(s)$ is antisymmetric.

3.2. A spectral collocation method for z. We consider a semi-implicit method for

$$z_t = iz_{ss} \mp \frac{2i\bar{z}}{1 \pm |z|^2}z_s^2, \tag{3.12}$$

where we treat the linear term on the right-hand side, iz_ss, implicitly, and the nonlinear term explicitly. We use a Chebyshev spectral collocation method [8], with nodes s_i:

$$s_i = L\cos\left(\frac{i\pi}{N}\right), \qquad i = 0, \cdots, N,$$

and approximate z by a polynomial of the form

$$z(s,t) \approx \sum_{k=0}^{N} a_k(t)T_k(s/L),$$

where $T_x(s) = \cos(k\arccos s)$ is the Chebyshev polynomial of degree k. The coefficients $\{a_k\}_{k=0}^N$ are obtained using the fast Fourier transform (FFT) [15].

For time evolution, we have chosen a second order, semi-implicit Backward Differentiation Formula (BDF) [22, 2]:

$$\frac{1}{2\Delta t}\left[3U^{n+1} - 4U^n + U^{n-1}\right] = iU_{ss}^{n+1} + 2\mathcal{N}(U^n, t^n) - \mathcal{N}(U^{n-1}, t^{n-1}), \tag{3.13}$$

where we denote by $\mathcal{N}(U,t)$ the nonlinear term on the right-hand side of (3.12). The BDF is particularly suited for this problem, as it imposes a very strong decay in the high frequency modes.

Boundary conditions of Dirichlet or Neumann type can be easily implemented:

1. Dirichlet boundary condition:

$$
\begin{cases}
u(-L,t) = u_1(t), \\
u(+L,t) = u_2(t)
\end{cases}
\longleftrightarrow
\begin{cases}
\sum_{k=0}^{N}(-1)^k a_k^{n+1} = u_1(t^{n+1}) \\
\sum_{k=0}^{N} a_k^{n+1} = u_2(t^{n+1}).
\end{cases}
\tag{3.14}
$$

2. Neumann boundary condition:

$$
\begin{cases}
u_s(-L,t) = u_1(t) \\
u_s(+L,t) = u_2(t)
\end{cases}
\longleftrightarrow
\begin{cases}
\dfrac{1}{L}\sum_{k=0}^{N}(-1)^{k+1}k^2 a_k^{n+1} = u_1(t^{n+1}) \\
\dfrac{1}{L}\sum_{k=0}^{N} k^2 a_k^{n+1} = u_2(t^{n+1}).
\end{cases}
\tag{3.15}
$$

We use a spectral filter, and set equal to zero all those coefficients a_k^{n+1} whose modulus is smaller than a given ε [21]. Specifically, we have made $a_k \equiv 0$ whenever $|a_k^{n+1}| < 10^{-14}$.

For scheme (3.13) we need two initial conditions, one at time $t = t^0$, which is known, and the other one at $t = t^1$. We obtain $U(s,t^1) \approx u(s,t^1)$ using semi-implicit Backward Euler, and Richardson extrapolation.

3.3. Projected second order boundary condition. In order to compare the finite-difference and the pseudo-spectral method, we have projected the same second order boundary condition we used for $\mathbf{T}$: We approximate $\mathbf{T}(L,t^{n+1})$ as in (2.12):

$$
\tilde{\mathbf{T}}^{n+1}(L) = \tilde{\mathbf{A}} + 2c_0\sqrt{t^{n+1}}\frac{\Im[\tilde{\mathbf{B}}e^{iL^2/4t^{n+1}}]}{L}, \quad \mathbf{T}^{n+1}(L) = \frac{\tilde{\mathbf{T}}^{n+1}(L)}{(\pm\tilde{\mathbf{T}}^{n+1}(L) \circ_\pm \tilde{\mathbf{T}}^{n+1}(L))^{\frac{1}{2}}};
$$

and project it over $\mathbb{C}$, so

$$
z^{n+1}(L) = \frac{T_1^{n+1}(L)}{1+T_3^{n+1}(L)} + i\frac{T_2^{n+1}(L)}{1+T_3^{n+1}(L)}.
$$

$\tilde{\mathbf{A}}$ and $\tilde{\mathbf{B}}$ are computed also using the asymptotic expansion for $\mathbf{T}$:

$$
\tilde{\mathbf{A}} \equiv \mathbf{T}(L,t_0) + 2c_0\sqrt{t_0}\frac{\mathbf{e}_2(L,t_0)}{L},
$$
$$
\tilde{\mathbf{B}} \equiv (\mathbf{e}_1(L,t) - i\mathbf{e}_2(L,t))e^{-iL^2/4t},
$$

where $\mathbf{T}(L,t_0)$, $\mathbf{e}_1(L,t_0)$ and $\mathbf{e}_2(L,t_0)$ are obtained from (3.2), (3.6) and (3.7), respectively.

We choose the same parameters as in the finite difference case, i.e., $c_0 = 0.2$. Only the results for the Euclidean case will be given, since the results for the hyperbolic case are virtually identical for this value of c_0. To measure the accuracy of our results, we compute the curvature as a function of space and time, and compare with the exact value $\frac{c_0}{\sqrt{t}}$. Thus, the smaller the time that we reach with correct curvatures, the better we will consider the results to be. To illustrate the need for high resolution, we show in figure 3.1 the curvature c obtained for $t = 0.04$. The theoretical value is $c_0/\sqrt{t} = 1$. As can be seen, when $N = 512$, the accuracy is completely lost. In contrast, when $N = 2048$, the error is of the order of 10^{-8}.

In all our numerical simulations, even for big N, we have found no restriction for $|\Delta t|$, so there is evidence that the method is unconditionally stable. Nevertheless, since the method is of order two, diminishing $|\Delta t|$ can improve greatly the results,
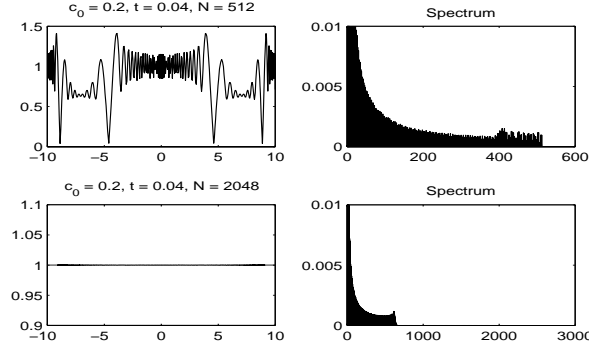
FIG. 3.1. *Curvature and spectrum of the exact $z(s, 0.01)$, when N is too small ($N = 512$) and when N is big enough ($N = 2048$).*
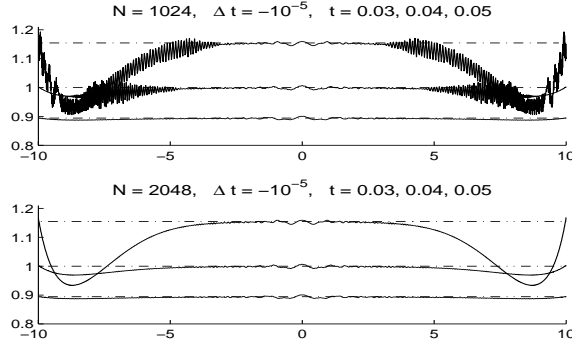

FIG. 3.2. *Curvature, for $|\Delta t| = 10^{-5}$. When $N = 1024$, the spectrum has overflowed and there appears noise, because of the lack of frequencies. With $N = 2048$, this noise have disappeared.*

provided N is large enough. In figure 3.2, we plot the curvature for $N = 1024$ and $N = 2048$, at $t = 0.03$, $t = 0.04$ y $t = 0.05$. For $N = 1024$, the noise indicates that the resolution is not high enough. Doubling the number of collocation points ameliorates the situation. Reducing the time step is not enough to remove the oscillations: using $\Delta t = -10^{-6}$, the results at the same time instants are practically exact for $N = 2048$, but, for $N = 1024$ the noise has not disappeared, as we see in Figure 3.3.

In order to study the cusp-formation at $t = 0$, we hade developed an adaptive methodology, both in time and space. A simple strategy is to simply duplicate the number of Chebyshev nodes whenever the derivative of z develops, high frequency components. Specifically, if we write

$$z_s(s) = \sum_{k=0}^{N} b_k T_k(s/L),$$

we duplicate the number of nodes when

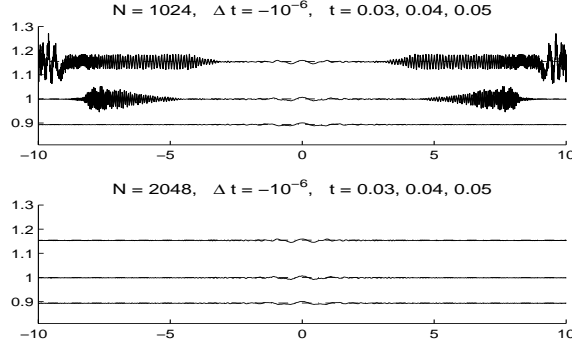$$\max_{k \in [\frac{3N}{4}, N]} |b_k| > 2 \cdot 10^{-4}. \tag{3.16}$$

FIG. 3.3. *Curvature, for* $|\Delta t| = 10^{-6}$. *Diminishing* Δt *is only useful when the number of frequencies is satisfactory.*

Whenever we duplicate the frequencies, we divide Δt by 4.

Using this strategy, we have solved the equation starting with $N = 1024$, and $\Delta t = -2 \times 10^{-6}$, up to $N = 16384$.

Since our method is only second order in time, we would need a priori small $|\Delta t|$ in order to decrease the numerical errors. In Figure 3.4, we plot the curvature
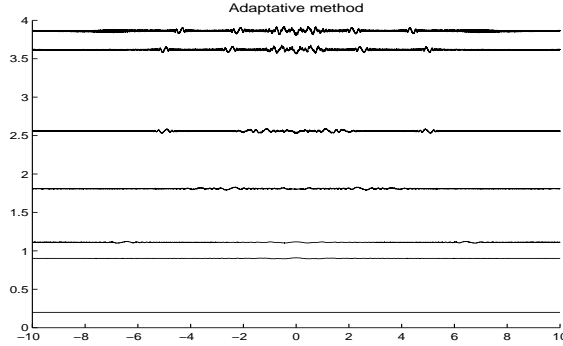
FIG. 3.4. *Adaptive method, with approximated boundary condition, from* $N = 1024$ *to* $N = 16384$.

in those instants where we have duplicated number of Chebyshev nodes, that is, at $t = 4.91 \cdot 10^{-2}$, $t = 3.24 \cdot 10^{-2}$, $t = 1.22 \cdot 10^{-2}$ and $t = 6.09 \cdot 10^{-3}$, and gone down up to $t = 2.67 \cdot 10^{-3}$. Note that this means that the curvature has been increased by a factor of 20, and the energy by a factor of 400.

3.3.1. Self-similarity boundary conditions. Since we are trying to approximate the self-similar solutions, i.e., $z(s, t) = z(s/\sqrt{t}, 1)$, it seems natural to introduce this condition on the boundary. Upon differentiation, we get 21

$$z_t(s, t) = -\frac{s}{2t} z_s(s, t), \tag{3.17}$$

which can be translated into the following boundary conditions:

$$\frac{z^{n+1}(L) - z^{n-1}(L)}{2\Delta t} = -\frac{L}{2t^n} z_s^n(L),$$
$$\frac{z^{n+1}(-L) - z^{n-1}(-L)}{2\Delta t} = \frac{L}{2t^n} z_s^n(-L).$$

This choice of the boundary condition produces good results. However, for accuracy reasons, for small t, we need to choose Δt small enough to avoid numerical artifacts on the boundary. This is illustrated in figure 3.5, where we show what happens on the boundary when Δt is chosen to be too large.
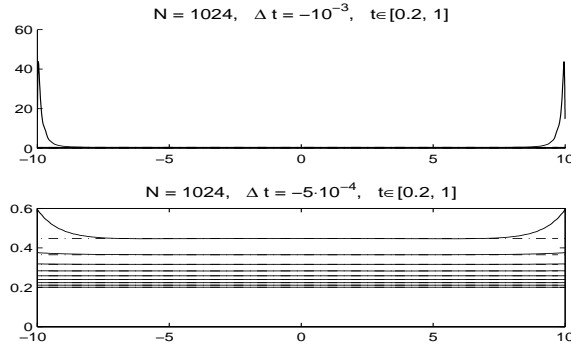

FIG. 3.5. *Curvature for too big* Δt. *When* $\Delta t = -10^{-3}$, *curvature explodes at* $s = \pm L$ *around* $t = 0.2$. *With* $\Delta t = -5 \cdot 10^{-4}$, *there is a good improvement.*
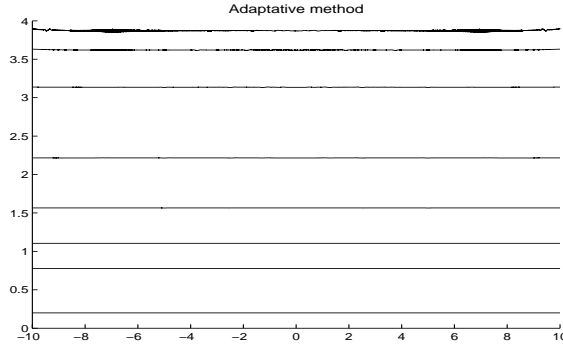

FIG. 3.6. *Adaptive method, with self-similar boundary conditions, from* $N = 1024$ *till* $N = 16384$.

In Figure 3.6, we have implemented an adaptive method, starting from $N = 1024$, $\Delta t = -2 \cdot 10^{-6}$. Representing $z_s(s) = \sum_{k=0}^{N} b_k T_k(s/L)$, we have duplicated the frequencies when

$$\max_{k \in [\frac{3N}{4}, N]} |b_k| > 5 \cdot 10^{-5}; \tag{3.18}$$

i.e., at $t = 6.61 \cdot 10^{-2}$, $t = 3.23 \cdot 10^{-2}$, $t = 1.63 \cdot 10^{-2}$ and $t = 8.15 \cdot 10^{-3}$. With $N = 16384$, the results are still valid for much smaller times; in the figure we have also shown the curvature when $t = 4.07 \cdot 10^{-3}$, $t = 3.05 \cdot 10^{-3}$ and $t = 2.67 \cdot 10^{-3}$, multiplying almost by 20 the initial curvature. Observe that, in comparison with Figure 3.4, the results of Figure 3.6 are much cleaner.

3.4. Radiation boundary condition. We derive another boundary condition, that aims at capturing the correct flow of energy through the boundary at $s = \pm L$. For this, we consider the Hasimoto transform, $\psi = c \exp\left(i \int_0^s \tau(s', t) ds'\right)$. From (3.4) and (3.5), it follows that

$$\psi = \frac{2|z_s|}{1 \pm |z|^2} \exp\left[i \int_0^s \left(\frac{2(yx_s - xy_s)}{\pm 1 + x^2 + y^2} + \frac{x_s y_{ss} - y_s x_{ss}}{x_s^2 + y_s^2}\right) ds'\right].$$

Now,

$$\frac{x_s y_{ss} - y_s x_{ss}}{x_s^2 + y_s^2} = \frac{\dfrac{y_{ss}}{x_s} - \dfrac{y_s x_{ss}}{x_s^2}}{1 + \left(\dfrac{y_s}{x_s}\right)^2} = \frac{\partial}{\partial s} \arctan\left(\frac{y_s}{x_s}\right),$$

so

$$\psi = \frac{2|z_s|}{1 \pm |z|^2} \exp\left\{i \int_0^s \left[\frac{2(yx_s - xy_s)}{\pm 1 + x^2 + y^2} + \frac{\partial}{\partial s} \arctan\left(\frac{y_s}{x_s}\right)\right] ds'\right\}$$

$$= \frac{2|z_s|}{1 \pm |z|^2} \exp\left[i \arctan\left(\frac{y_s}{x_s}\right) - i \arctan\left(\frac{y_s(0)}{x_s(0)}\right)\right] \exp\left[i \int_0^s \frac{2(yx_s - xy_s)}{\pm 1 + x^2 + y^2} ds'\right]$$

$$= \frac{2z_s}{1 \pm |z|^2} \exp\left[i \int_0^s \frac{2(yx_s - xy_s)}{\pm 1 + x^2 + y^2} ds'\right] \exp\left[-i \arctan\left(\frac{y_s(0)}{x_s(0)}\right)\right]. \tag{3.19}$$

At $s = \pm L$, we know that $\psi(\pm L, t) = \dfrac{c_0}{\sqrt{t}} e^{i\frac{L^2}{4t}}$. From this, it follows that

$$\frac{c_0}{\sqrt{t}} e^{i\frac{L^2}{4t}} = \left\{\frac{2z_s}{1 \pm |z|^2} \exp\left[i \int_0^s \frac{2(yx_s - xy_s)}{\pm 1 + x^2 + y^2} ds'\right] \exp\left[-i \arctan\left(\frac{y_s(0)}{x_s(0)}\right)\right]\right\}_{s = \pm L},$$

resulting

$$z_s(\pm L, t) = \left\{\frac{1 \pm |z|^2}{2} \frac{c_0}{\sqrt{t}} e^{i\frac{s^2}{4t}} \exp\left[-i \int_0^s \frac{2(yx_s - xy_s)}{\pm 1 + x^2 + y^2} ds'\right] \exp\left[i \arctan\left(\frac{y_s(0)}{x_s(0)}\right)\right]\right\}_{s = \pm L}. \tag{3.20}$$

We can give the boundary condition as

$$z_s^{n+1}(\pm L) = \left\{\frac{1 \pm |z|^2}{2} \frac{c_0}{\sqrt{t}} e^{i\frac{s^2}{4t}} \exp\left[-i \int_0^s \frac{2(yx_s - xy_s)}{\pm 1 + x^2 + y^2} ds'\right] \exp\left[i \arctan\left(\frac{y_s(0)}{x_s(0)}\right)\right]\right\}_{\substack{s = \pm L \\ t = t^n}},$$

which makes the scheme be first order. To obtain a second order scheme, we do

$$z_s^{n+1}(\pm L) = 2\left\{\frac{1 \pm |z|^2}{2} \frac{c_0}{\sqrt{t}} e^{i\frac{s^2}{4t}} \exp\left[-i \int_0^s \frac{2(yx_s - xy_s)}{\pm 1 + x^2 + y^2} ds'\right] \exp\left[i \arctan\left(\frac{y_s(0)}{x_s(0)}\right)\right]\right\}_{\substack{s = \pm L \\ t = t^n}}$$

$$- \left\{\frac{1 \pm |z|^2}{2} \frac{c_0}{\sqrt{t}} e^{i\frac{s^2}{4t}} \exp\left[-i \int_0^s \frac{2(yx_s - xy_s)}{\pm 1 + x^2 + y^2} ds'\right] \exp\left[i \arctan\left(\frac{y_s(0)}{x_s(0)}\right)\right]\right\}_{\substack{s = \pm L \\ t = t^{n-1}}}. \tag{3.21}$$

Notice that for unperturbed solutions or for solutions perturbed with an even perturbation, we have

$$\exp\left[i\arctan\left(\frac{y_s(0)}{x_s(0)}\right)\right] = 1.$$

We have found the scheme to be unconditionally stable, and that the results in the backward case are as good as those obtained with the boundary condition described in section 3.3.1. What is more important, this boundary condition seems to work extraordinarily well for the progressive case. In Figure 3.7, considering $t^0 = 1$, we have solved the equation up to $t = 2$. The results in this case are excellent.
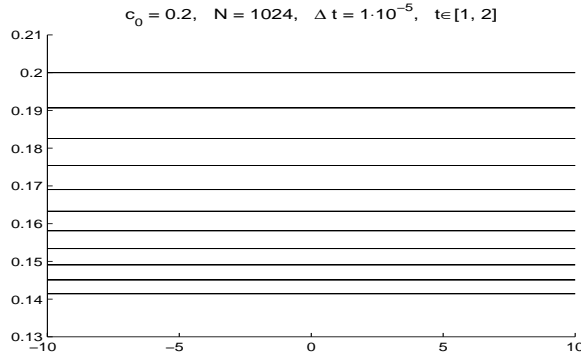

FIG. 3.7. *Forward case, using the third boundary conditions. In comparison with figure 2.7, the results are excellent.*

3.5. Forward case in time. The pseudo-spectral method, together with the last boundary condition, allows to give a complete treatment of the forward case, unlike with the finite differences.

We consider the following initial value problem:

$$\begin{cases} z_t = iz_{ss} \mp \dfrac{2i\bar{z}}{1 \pm |z|^2}z_s^2, \\ z(s,t) = a^1 s\chi_{[0,+\infty)}(s) + a^2 s\chi_{(-\infty,0]}(s). \end{cases}$$

Once c_0 is fixed, we can consider take a^1 and a^2 as the respective projections of $\mathbf{A}^1(c_0)$ and $\mathbf{A}^2(c_0)$ used in (2.17), i.e.,

$$a^1 = \frac{\sqrt{\pm(1 - e^{\mp c_0^2\pi})}}{1 + e^{\mp\frac{c_0^2}{2}\pi}}, \qquad\qquad a^2 = -\frac{\sqrt{\pm(1 - e^{\mp c_0^2\pi})}}{1 + e^{\mp\frac{c_0^2}{2}\pi}}. \qquad (3.22)$$

Therefore, discretizing $[-L, L]$ in $s_i = L\cos(i\pi/N)$, with $i = 0, \cdots, N$, the numerical initial datum is

$$\begin{cases} z_i^0 \equiv z(s_i, 0) \equiv a^+, & i \in \{0, \cdots, \frac{N}{2} - 1\}, \\ z_{N/2}^0 \equiv z(0,0) \equiv 0, \\ z_i^0 \equiv z(s_i, 0) \equiv a^-, & i \in \{\frac{N}{2} + 1, \cdots, N\}. \end{cases}$$

This boundary condition is not adequate for large t; when the information reaches the boundary, it is reflected back into the domain, creating a fractal phenomenon, as illustrated in figure 3.8, where we show the case $c_0 = 0.2$, $N = 16384$, $L = 50$ and $t = 10$. If, however, we consider for the same parameters a much smaller time,
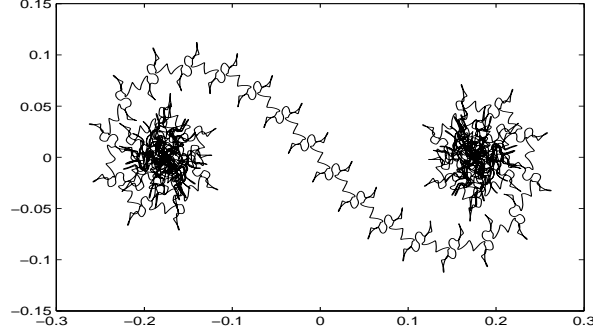

FIG. 3.8. *Fractal creation*

for instance $t = 0.3$, we observe in Figure 3.9 that the information, even if it has already reached the boundary, has only partially rebounded. Thus, in spite of the great noise at the extremes, if we make a zoom of the central subinterval $[-10, 10]$, the achieved accuracy is notorious. Therefore, we will consider the portion of the
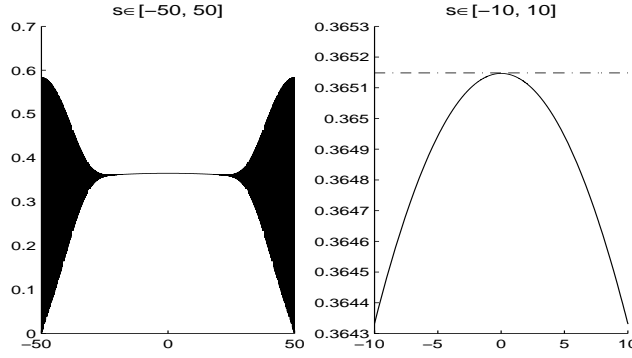

FIG. 3.9. *Starting from $t = 0$, with $\Delta t = 10^{-5}$, at $t = 0.3$ the information has reached the boundary and partially rebounded. Nevertheless, in $s \in [-10, 10]$, the error of the curvature is smaller that $9 \cdot 10^{-4}$, so that portion of curve is well suited to be our new initial datum.*

curve corresponding to that subinterval as our new initial datum.

Now, we know $z(s, 0.3)$ at $s_i = 50 \cos(i\pi/16384)$, $i = 0, \cdots, 16384$, and have to interpolate spectrally $z(s, 0.3)$ in the new initial nodes $\tilde{s}_i$, which we have chosen as

$$\tilde{s}_i = 10 \cos\left(\frac{i\pi}{1024}\right), \qquad i = 0, \cdots, 1024.$$

Therefore, we have to interpolate z in $1024 + 1$ points belonging to $[-10, 10]$; this can

be done directly from the expression for z as a function of the coefficients a_k:

$$z(\tilde{s}_i) = \sum_{k=0}^{N} a_k T_k \left(\frac{\tilde{s}_i}{L} \right) = \sum_{k=0}^{N} a_k \cos \left(k \arccos \left(\frac{\tilde{s}_i}{L} \right) \right).$$
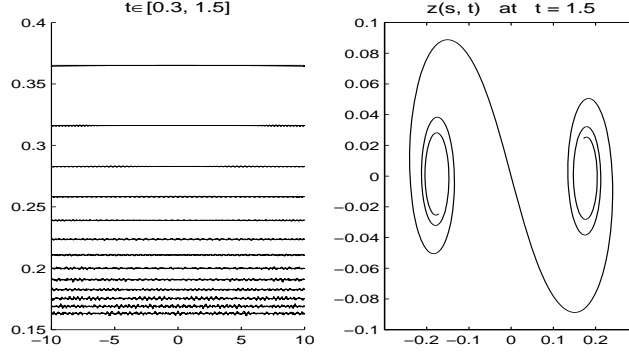

FIG. 3.10. *Taking as initial datum the right side of figure 3.9, we have advanced till $t = 1.5$, with $\Delta t = 10^{-5}$ and the third boundary condition. At the right side, we have drawn the curve obtained at $t = 1.5$.*

In Figure 3.10, we have calculated the evolution of z with that new initial datum and the third boundary condition in $s = \pm 10$. Although there appears some noise, because the new initial datum is not exact, the results are acceptable.

To finish, let us mention also that, unlike in the finite difference case, there are no problems when $\Delta t \to 0$ in any of the two stages.

4. A stability result. In the previous sections, we have described several schemes to approximate numerically the self-similar solutions of

$$\mathbf{X}_t = \mathbf{X}_s \wedge_{\pm} \mathbf{X}_{ss} \tag{4.1}$$

and

$$\mathbf{T}_t = \mathbf{T} \wedge_{\pm} \mathbf{T}_{ss}, \tag{4.2}$$

which are characterized by

$$c(s,t) = \frac{c_0}{2}, \qquad \tau(s,t) = \frac{s}{2t}. \tag{4.3}$$

Since we could not work with all $\mathbb{R}$, we have bounded ourselves to $s \in [-L, L]$, considering different boundary conditions at $s = \pm L$. It is clear that these boundary conditions, from a numerical point of view, will never be completely exact; even in the best of the cases there will be some errors, although they may be as small as the machine precision. Thus, we can consider all our experiments to be perturbation of the exact solutions for $\mathbf{X}$, $\mathbf{T}$ and the projection of $\mathbf{T}$, z.

In the previous sections, we have seen that the stability of all the experiments is good, no matter wether we consider very rough boundary conditions, as fixing $\mathbf{T}(s,t)$ at $\pm L$ or more elaborated ones. Thus, before concluding this paper, it is interesting

to mention for completeness some recent results by Banica and Vega [3, 4], that guarantee theoretically this stability, at least for small perturbations.

Equations (4.1) and (4.2) are closely related to the cubic Schrödinger equation or non-linear Schrödinger equation (NLS). Indeed, by means of Hasimoto's transforms

$$\psi(s,t) = c(s,t)\exp\left(i\int_0^s \tau(s',t)ds'\right),\qquad(4.4)$$

we obtain the NLS [20] [6],

$$i\psi_t + \psi_{ss} \pm \frac{1}{2}[|\psi|^2 + A(t)]\psi = 0,\qquad(4.5)$$

The term $A(t)$ can be immediately absorbed by means of a change of variable $\Psi = \psi\exp\left(\mp i/2\int_0^t A(t')dt'\right)$

$$i\psi_t + \psi_{ss} \pm \frac{1}{2}|\psi|^2\psi = 0.\qquad(4.6)$$

The case with the $+$ sign is known as the focussing case, the cubic Schrödinger equation being denote NLS$^+$; this corresponds to the Euclidean case of (1.8) and (1.9). With the $-$ sign, corresponding to the hyperbolic case of (1.8) and (1.9), we have the defocussing case, the Schrödinger cubic being denoted as NLS$^-$. The Schrödinger cubic equation appears in many contexts [12], as certain non-linear optics phenomena, wave packets in water and plasma, etc...

Coming back to (4.5), in our current problem, from (4.3),

$$\psi(s,t) = \frac{c_0}{\sqrt{t}}e^{is^2/4t}.\qquad(4.7)$$

If we choose $A(t) = -\frac{c_0^2}{t}$, we get a solution of (4.5), with $\psi(0,s) = \sqrt{i}c_0\delta$, being δ Dirac's distribution. Thus, going from $\mathbf{X}$ and z to ψ means to trivialize the problem in a certain way, since, for every $t > 0$, we know the explicit equation.

Now, the solutions (4.7) of the Schrödinger cubic equation (4.5) that we are considering satisfy trivially

$$\int_{\mathbb{R}}|\psi(s,t)|^2 ds = \int_{\mathbb{R}}|\psi(0,s)|^2 ds.$$

Therefore, from this point of view, our solutions have infinite energy. Nevertheless, Banica and Vega [3, 4] have proved that, under certain renormalizations, the solutions have finite energy. Indeed, starting from

$$i\psi_t(s,t) + \psi_{ss}(s,t) - \frac{1}{2}\left[|\psi(s,t)|^2 - \frac{c_0^2}{t}\right]\psi(s,t) = 0,$$

we make the change $u(s,t) = \psi(\sqrt{2}s, 2t)$ in order to absorb the constant $\frac{1}{2}$, obtaining

$$iu_t(s,t) + u_{ss}(s,t) \pm \left(|u(s,t)|^2 - \frac{c_0^2}{2t}\right)u(s,t) = 0.\qquad(4.8)$$

Applying to this last expression the following conformal transform

$$u(s,t) = Tv(s,t) = \frac{e^{i\frac{s^2}{4t}}}{t^{1/2}}v\left(\frac{s}{t}, \frac{1}{t}\right),\qquad(4.9)$$

and evaluating in $(s,t) = \left(\frac{s}{t}, \frac{1}{t}\right)$, we get

$$v_t(s,t) = -iv_{ss}(s,t) \mp \frac{i}{t}\left(|v(s,t)|^2 - \frac{c_0^2}{2}\right)v(s,t). \qquad (4.10)$$

Therefore, when $0 < t < t_0$, u is solution of

$$\begin{cases} iu_t(s,t) + u_{ss}(s,t) \pm \left(|u(s,t)|^2 - \frac{c_0^2}{2t}\right)u(s,t) &=& 0, \\ u(t_0,s) &=& \frac{c_0}{\sqrt{2t_0}}e^{i\frac{s^2}{4}t_0} + u_1(s), \end{cases} \qquad (4.11)$$

if and only if v is a solution, when $1/t_0 < t < \infty$, of

$$\begin{cases} v_t(s,t) &=& -iv_{ss}(s,t) \mp \frac{i}{t}\left(|v(s,t)|^2 - \frac{c_0^2}{2}\right)v(s,t), \\ v(s,1/t_0) &=& \frac{c_0}{2} + v_0, \end{cases} \qquad (4.12)$$

with $v_0(s) = T^{-1}u_1(s)$. Notice that, due to the conformal transform, the case $t \to 0^+$ gets transformed into $t \to +\infty$. Moreover, our exact unperturbed solutions are now constant solutions of u.

There is an energy naturally associated to (4.12),

$$E(t) = \frac{1}{2}\int |v_s(s,t)|^2 ds \mp \frac{1}{4t}\int \left(|v(s,t)|^2 - \frac{c_0^2}{2}\right)^2 ds. \qquad (4.13)$$

Therefore, if v is a solution of (4.12), we get

$$\frac{\partial}{\partial t}E(t) \mp \frac{1}{4t^2}\int \left(|v(s,t)|^2 - \frac{c_0^2}{2}\right)^2 ds = 0. \qquad (4.14)$$

This last equation implies, in the defocussing situation corresponding to the hyperbolic case, that the energy does not grow when $t \to \infty$. As a consequence of (4.14), Banica and Vega proved in [3] the following theorem for the defocussing case:

THEOREM 4.1.

For every $t_0 > 0$ and for every $v_0 \in \mathcal{H}^1$, there exists a unique solution of the initial value problem (4.12), with

$$v - \frac{c_0}{2} \in \mathcal{C}((1/t_0, \infty), \mathcal{H}^1).$$

Banica and Vega also proved that

$$\liminf_{t \to \infty} \frac{1}{t}\int \left(|v(s,t)|^2 - \frac{c_0^2}{2}\right)^2 ds = 0,$$

which implies that u, in the defocussing case, when $0 < t < t_0$, satisfies

$$\liminf_{t \to 0} \||t|u(t)|^2 - c_0^2\|_2 = 0.$$

This last expression is already a stability result for the singular solution $\frac{c_0}{\sqrt{2t_0}}e^{i\frac{s^2}{4}t_0}$ of (4.11).

Finally, in the defocussing case, writing in terms of the geometric quantities c and τ the corresponding energy to (4.4), which is a solution of (4.5), we get

$$\widetilde{E}(t) = \frac{t^2}{4\sqrt{2}} \int_{-\infty}^{+\infty} \left(c_s^2(s,t) + c^2(s,t) \left(\frac{s}{2t} - \tau(s,t) \right)^2 \right) ds$$
$$+ \frac{1}{16\sqrt{2}} \int_{-\infty}^{+\infty} [tc^2(s,t) - c_0^2]^2 ds, \tag{4.15}$$

and, hence,

$$\frac{d}{dt} \widetilde{E}(t) - \frac{1}{16\sqrt{2}\, t} \int_{-\infty}^{+\infty} [tc^2(s,t) - c_0^2]^2 ds = 0 \tag{4.16}$$

and

$$\liminf_{t \to 0} \| t|c|^2 - c_0^2 \|_2 = 0. \tag{4.17}$$

Observe that our solutions are precisely such that $\widetilde{E}(t) = 0$, for all $t > 0$.

In the focussing setting (i.e. the case of the sphere) the stability is much more delicate. In [4], and under a smallness assumption in the curvature c_0, they construct a global solution such that $E(t)$ given in (4.13) is finite. The main difficulty comes from the long range character of the non-linear potential that appears in (4.12). This implies the existence of a logarithmic phase that has as a consequence the non existence of the limit at infinity for the solutions. However they also prove, this time in the focussing case, that this logarithmic divergence disappears when the tangent vector T is computed, so that there is stability for T. Remember that in order to compute T one has to integrate once the curvature and twice the torsion. Therefore thanks to the oscillations the integrals converge without any difficulty.

5. Conclusions. In this paper, we have tried to reproduce numerically the behavior of the self-similar solutions of

$$\mathbf{X}_t = \mathbf{X}_s \wedge_\pm \mathbf{X}_{ss} \tag{5.1}$$

and

$$\mathbf{T}_t = \mathbf{T} \wedge_\pm \mathbf{T}_{ss}, \tag{5.2}$$

which develop a singularity at finite time. These solutions, characterized by

$$c(s,t) = \frac{c_0}{2}, \qquad \tau(s,t) = \frac{s}{2t}, \tag{5.3}$$

form a one-parameter family, where c_0 is precisely the family parameter.

The singularities happen at $t = 0$, going backwards in time, but, since both (5.1) and (5.2) are time-reversible, we could consider an equivalent problem, where we advance in time and the singularity happens.

In Section 2, we have given a finite-difference scheme to study the self-similar solutions of $\mathbf{T}$. $\mathbf{T}$ determines completely $\mathbf{X}$, except for a constant, determined by $\mathbf{X}(0,t) = 2c_0\sqrt{t}(0,1,0)$. We have studied mainly the backward case: starting from $t = 1$, we have tried to reproduce the formation of the singularity. Since we cannot consider all $\mathbb{R}$, we have bounded ourselves to $s \in [-L, L]$, being necessary to give

boundary conditions at $s = \pm L$. From the asymptotics of Theorem 1.1 for $\mathbf{T}(s, 1)$, we have deduced two approximated boundary conditions, depending on whether we choose the leading term of $\mathbf{T}(s, 1)$, or the first two terms in the expansion.

Considering $\mathbf{T}(s, 1)$ constant at $s = \pm L$ gives us good results from a qualitative point of view: the energy is preserved with several precision digits and we get also the approximated value of $c(0, t)$, even for small times. Thus, the finite energy tends to concentrate on the origin, approximating the formation of the singularity at $t = 0$. In the exact solution, the energy was infinite for all t, but the behavior is the same: all the energy tends to concentrate at $s = 0$.

Since the bigger is L, the smaller are the times for which we recover $c(0, t)$, there seems to be evidence that we could approximate the exact problem by making L tend to infinity. It would be very interesting to prove this analytically.

The second boundary condition is obtained considering the first non-constant term in the asymptotics of $\mathbf{T}(s, 1)$, and that $\mathbf{T}(s, t) = \mathbf{T}(s/\sqrt{t}, 1)$. For not too big L and provided that Δs is small enough, it allows us to recover the solutions with big accuracy even for small times; moreover, not only for $s = 0$, but for all s. Nevertheless, since $|\Delta t| = \mathcal{O}(\Delta s^2)$, this is quite expensive from a computational point of view.

When L is bigger, a uniform distribution of the nodes is not adequate, because there is a lack of resolution for s near the boundary. That suggests that we use an alternative node distribution, given by the Chebyshev nodes, which are distributed in a much more suitable way. Since, with an explicit scheme, we would have now a $|\Delta t| = \mathcal{O}(N^{-4})$ restriction, we have projected stereographically $\mathbf{T}$ over $\mathbb{C}$, obtaining

$$z_t = iz_{ss} \mp \frac{2i\bar{z}}{1 \pm |z|^2} z_s^2. \tag{5.4}$$

We have implemented an implicit-explicit method in time, with a pseudo-spectral method in space, considering different boundary conditions. This method has several interesting advantages: its stability is much better for a given N; it allows considering much bigger L; it allows implementing boundary conditions that do not need external information and $\mathbf{X}$ can be recovered immediately with spectral accuracy. Since designing an adaptive version, i.e., refining the grid when necessary, is natural and straight-forward, the method is globally much more efficient. Lastly, it allows to make a full treatment of the forward case: starting from a singular datum at $t = 0$, we can recover the solutions in two stages, by adapting at $t = \varepsilon$ adequate boundary conditions.

Finally, let us mention that all the experiments we have done give evidence of the stability of equations (5.1), (5.2) and (5.4) from a numerical point of view. Indeed, when giving the boundary conditions at $s = \pm L$, it is impossible to do it exactly and we will always be introducing some perturbations; when, for instance, we fix $\mathbf{T}(s, t)$ to be constant at $s = \pm L$, these perturbations will be quite big. Even if we calculated the exact value of $\mathbf{X}$, $\mathbf{T}$ or z at $s = \pm L$, there would always be a tiny error attributable to machine precision. Therefore, in Section 4, we have mention a recent stability result by Banica and Vega, concerning the self-similar solutions we have studied. This offers, somehow, a theoretical support to this paper.

REFERENCES

[1] R. J. Arms and F. R. Hama, *Localized-induction concept on a curved vortex and motion of an elliptic vortex ring*, Phys. Fluids, 8 (1965), pp. 553–559.

[2] U. M. Ascher, S. J. Ruuth, and B. T. R. Wetton, *Implicit-explicit methods for time-dependent partial differential equations*, SINUM, 32 (1995), pp. 797–823.

[3] V. Banica and L. Vega, *On the dirac delta as initial conditions for non-linear schrödinger equations*, Ann. I. H. Poincaré, An. Non Lin., 25 (2008), pp. 697–711.

[4] ———, *On the stability of a singular vortex dynamics*, Comm. Math. Phys., (to appear).

[5] G. K. Batchelor, *An Introduction to the Fluid Dynamics*, Cambridge Mathematical Library, Cambridge University Press, 1967.

[6] T. F. Buttke, *A numerical study of superfluid turbulence in the self-induction approximation*, PhD thesis, University of California, Berkeley, 1986.

[7] ———, *A numerical study of superfluid turbulence in the self-induction approximation*, J. of Com. Phys., 76 (1988), pp. 301–326.

[8] C. Canuto, M. Y. Hussaini, A. Quarteroni, and T. A. Zang, *Spectral methods in fluid dynamics*, Springer Series in Computational Physics, Springer-Verlag, New York, 1988.

[9] I. Cimrák, *On the Landau-Lifshitz equation of ferromagnetism*, PhD thesis, Ghent University, 2005.

[10] L. S. Da Rios, *On the motion of an unbounded fluid with a vortex filament of any shape*, Rend. Circ. Mat. Palermo, 22 (1906), pp. 117–135. (in Italian).

[11] F. de la Hoz, *Self-similar solutions for the 1-d schrödinger map on the hyperbolic plane*, Math. Z., 257 (2007), pp. 61–80.

[12] P. G. Drazin and R. S. Johnson, *Solitons: an Introduction*, Cambridge University Press, 1992.

[13] W. E and X.-P. Wang, *Numerical methods for the landau-lifshitz equation*, SINUM, 38, pp. 1647–1665.

[14] B. Fornberg, *A practical Guide to Pseudospectral Methods*, Cambridge University Press, 1998.

[15] M. Frigo and S. G. Johnson, *The design and implementation of FFTW3*, Proceedings of the IEEE, 93 (2005), pp. 216–231. special issue on "Program Generation, Optimization, and Platform Adaptation".

[16] C. J. García-Cervera, W. E, and X.-P. Wang, *A gauss-seidel projection method for the landau-lifshitz equation*, J. Comp. Phys., 171 (2001), pp. 357–372.

[17] C. J. García-Cervera and A. M. Roma, *Adaptative mesh refinement for micromagnetics simulations*, IEEE Trans. Magn., 42 (2006), pp. 1648–1654.

[18] D. Gottlieb and S. A. Orszag, *Numerical Analysis of Spectral Methods: Theory and Applications*, SIAM, Philadelphia, Pennsylvania, 1997.

[19] S. Gutiérrez, J. Rivas, and L. Vega, *Formation of singularities and self-similar vortex motion under the localized induction approximation*, Comm. PDE volume, 28 (2003), pp. 927–968.

[20] H. Hasimoto, *A soliton on a vortex filament*, J. Fluid Mech., 51 (1972), pp. 477–485.

[21] T. Y. Hou, J. S. Lowengrub, and M. J. Shelley, *Removing the stiffness from interfacial flows with surface tension*, J. Comp. Phys., 114 (1994), pp. 312–338.

[22] J. D. Lambert, *Computational methods in ordinary differential equations*, John Wiley & Sons, London-New York-Sydney, 1973. Introductory Mathematics for Scientists and Engineers.

[23] L. D. Landau and E. M. Lifshitz, *On the theory of the dispersion of magnetic permeability in ferromagnetic bodies*, Phys. Z. Sowjetunion, 8 (1935), pp. 153–169.

[24] T. Lipniacki, *Quasi-static solutions for quantum vortex motion under the localized induction approximation*, J. Fluid Mech., 477 (2002), pp. 321–337.

[25] ———, *Shape-preserving solutions for quantum vortex motion*, Phys. Fluids, 15 (2003).

[26] P. G. Saffman, *Vortex dynamics*, Cambridge Monographs on Mechanics and Applied Mathematics, Cambridge University Press, New York, 1992.

[27] K. W. Schwarz, *Three-dimensional vortex dynamics in superfluid ^{4}he: line-line and line-boundary interactions*, Phys. Rev. B, 31 (1985), pp. 5782–5804.

[28] P. Sulem, C. Sulem, and C. Bardos, *On the continuous limit for a system of classical spins*, Comm. Math. Phys., 107 (1986), pp. 431–454.

[29] H. Werlé, *Onera photograph*, 1963.